ACS APPLIED NANO MATERIALS

www.acsanm.org Article

Self-Organized Tailoring of Faceted Glass Nanowrinkles for Organic Nanoelectronics

Maria Caterina Giordano, Federico di Sacco, Matteo Barelli, Giuseppe Portale,* and Francesco Buatier de Mongeot*

Cite This: *ACS Appl. Nano Mater.* 2021, 4, 1940−1950 Read Online

ACCESS | Metrics & More | Article Recommendations

ABSTRACT: Self-organized wrinkled templates are homogeneously fabricated over a large area (cm^2) glass substrates by defocused ion beam irradiation, demonstrating the capability to induce and modify at will the out-of-plane tilt of the nanofacets with selected slope. We identify a region of morphological instability which leads to faceting for incidence angles of the ion beam with respect to the surface, θ, in the range $15° \leq \theta \leq 45°$, while for normal incidence, $\theta = 0°$, and for grazing incidence at about 55−60° a flat morphology is achieved. The crucial parameter which controls the slope of the sawtooth profile is the local ion beam incidence angle on the facets which corresponds to the maximum erosion velocity. For $\theta = 30°$, improved lateral order of the templates is found which can be exploited for the anisotropic confinement of functional layers. Here, we highlight the crucial role of the 1D nanopatterned template in driving the anisotropic crystallization of spun-cast conductive polymer thin films in registry with the faceted nanogrooves. In response, anisotropic electrical transport properties of the nanopatterned film are achieved with overall improvement higher than 60% with respect to a flat reference, thus showing the potential of such transparent large-area templates in nanoelectronics, optoelectronics, and biosensing.

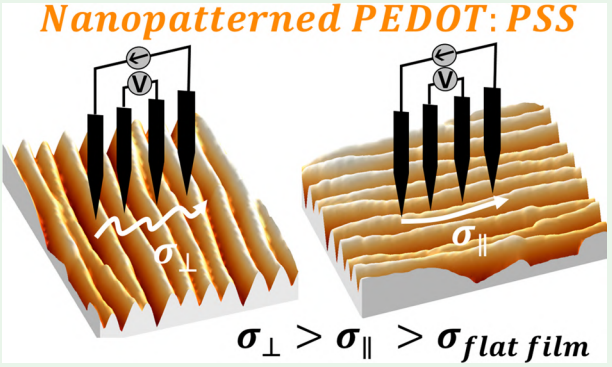

KEYWORDS: *Large area templates, nanoscale wrinkling, ion beam nanopatterning, self-organized nanofacets, organic electronics*

1. INTRODUCTION

The controlled nanopatterning of large area templates has recently attracted interest in a variety of fields, ranging from optoelectronics and biosensing to flexible nanoelectronics, where the development of fast and cost-effective solutions is crucial.[1−3] One aspect that has recently emerged deals with the possibility to tailor the electronic, optical and/or chemical properties over macroscopic scale by patterning surfaces in the form of periodic nanoscale oriented facets. This capability has recently enabled the effective tuning of the optoelectronic properties (band gap engineering) in two-dimensional (2D) materials grown on top of template substrates and in van der Waals heterostructures.[4−6] In a similar way the optical properties can be modified in subwavelength metasurfaces[7−9] based on plasmonic antennas featuring linear and nonlinear generation,[10−13] hyperbolic dispersion,[14] or on flat-optics gratings,[15,16] with a strong impact in nanophotonics, optical spectroscopies, and sensing.[17−19] In this context, the possibility to tailor the electrical conductivity at the nanoscale in plasmonic gratings[20,21] or the possibility to influence the nanostructure and crystallization of conducting polymeric thin films[22,23] is particularly appealing for applications such as biosensing,[24] medical diagnostic,[25] and flexible electronics.[26,27]

However, the nanofabrication of highly ordered nanogratings has been so far mainly relying on top-down lithographic approaches, characterized by a high resolution but practically limited in terms of capability to (i) produce out-of-plane tilted nanostructures and (ii) functionalize large area templates in a cost-effective way. In order to overcome the first issue, 3D nanostructures have been so far achieved via complex gray scale lithography processes[28] or, very recently, via electron beam lithography combined with tilted metal evaporation,[29] demonstrating tunable shape at the nanoscale but poor control on the out-of-plane tilt of the nanostructures.

In view of surface functionalization over a large area, a variety of self-assembled nanofabrication methods based either on direct interparticle interaction or on driven self-assembly have recently emerged,[30,31] demonstrating a strong potential for applications of pseudoperiodic planar assemblies of

Received: December 10, 2020
Accepted: February 2, 2021
Published: February 15, 2021

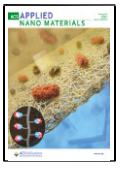

https://dx.doi.org/10.1021/acsanm.0c03290
ACS Appl. Nano Mater. 2021, 4, 1940−1950

nanostuctures. Alternatively, large-area arrays of nonplanar nanostructures can also be achieved by exploiting self-organization at surfaces under the destabilizing action of external driving forces, for example, induced by defocused ion beam irradiation.[32−35] Under this condition, periodic vertical patterning of the surface of different materials (either crystalline semiconductors and metals, or amorphous dielectric substrates) can be effectively induced over macroscopic areas. The nanoscale morphology can be tailored by simply acting on macroscopic parameters such as ion species, ion dose, ion incidence angle or substrate temperature. Periodic pattern formation in the case of amorphous substrates is determined by the orientation of the ion beam projection on the surface, and results from the interplay between the erosive action of the ion beam, and the relaxation of the corrugated profile by isotropic surface diffusion (both thermally activated and ion induced).[32,36,37] In the case of crystalline metal substrates[38,39] surface destabilization by the erosive action of the ion beam is instead counteracted by nonisotropic surface mass transport oriented along the thermodynamically favored crystallographic orientations. At variance with amorphous substrates for which the orientation of the periodic features is determined by the ion beam projection on the surface, crystalline metal substrate anisotropic diffusion favors recrystallization along the energetically most favored crystal orientations. In this way, it is possible to obtain the growth of out-of-plane oriented facets under specific conditions, such as controlled deposition and/or ion irradiation of crystalline surfaces.[36] More recently, very similar results have been achieved by irradiating semiconductor surfaces[34] above their recrystallization temperature[40−42] enabling several seminal experiments in nanophotonics and photochemistry which exploit high-aspect ratio crystalline nanostructures (e.g., nanocones, nanopits) characterized by oriented ridges that register with the crystallographic planes.[43,44] However, this approach is intrinsically limited to high-quality crystalline materials, opening a crucial issue in view of cost-effective applications in optoelectronics and flexible organic electronics, which are generally based on transparent low-cost substrates. The possibility to fabricate faceted periodic patterns with controlled periodicity, height, and slope at the surface of low cost amorphous substrates thus represents an open issue to be addressed in view of technological applications. A slope selection mechanism has been predicted at the surface of amorphous materials under grazing incidence sputtering for which geometrical shadowing plays a crucial role.[45] However, the experimental observations so far available for semiconductor surfaces describe the formation of relatively disordered patterns at high ion fluencies.[46,47] Recently, the intriguing possibility to induce an asymmetric faceting instability not related to shadowing has been theoretically predicted in continuum models which differ from the usual Kuramoto-Sivashinsky equation by the inclusion of a cubic nonlinearity.[48,49]

Here we demonstrate that ion-induced wrinkling can be engineered to fabricate large-area self-organized nanopatterns on a cm^2 scale with tailored facet orientation on a low-cost transparent dielectric substrate such as soda-lime glass, a material which is commonly employed as a functional template for many optoelectronic applications. The possibility to trigger the growth of a high-aspect ratio nanopattern via ion-induced solid-state wrinkling[50] is here pushed further, demonstrating the nanofabrication of one-dimensional (1D) arrays of out-of-plane oriented faceted ridges with tailored slope, deep submicrometer periodicity, and elongation exceeding several micrometers. Remarkably, we show the possibility to control at will the tilt of these quasi-1D nanoscale facets by simply changing the ion irradiation angle on the glass substrate, evidencing a peculiar slope selection mechanism.

The possibility to exploit large area nanorippled templates in cost-effective functional application in optoelectronics and plasmonics has been recently highlighted.[19,50,51] Here, we move a step further and demonstrate the possibility to exploit these 1D faceted glass templates to alter the structure of conducting polymeric thin films processed from solution. As an example, thin films of PEDOT:PSS, a prototypical material of relevance in organic flexible electronics,[52,53] are spun cast on top of the wrinkled nanopatterns and exhibit a measurable structural anisotropy in registry with the template pattern. As a consequence of this structural anisotropy, the electrical transport properties exhibit a remarkable anisotropic improvement of the electrical conductivity perpendicular to the periodic ridges, exceeding 60% when compared to a reference film deposited on flat substrates.

2. EXPERIMENTAL SECTION

2.1. Glass Nanopatterning and Morphological Characterization. Nanopatterning of low-cost glasses (soda lime) is performed by defocused ion beam sputtering (IBS) in a custom-made ultrahigh vacuum setup equipped with a gridded multiaperture ion source (TECTRA). This source generates a defocused Ar+ ion beam (5N purity), whose energy is fixed at 800 eV, while ion extraction is allowed by a metallic grid, polarized with a bias voltage $V_{grid} = -200$ V. Under this condition, the ion flux reaching the sample at normal incidence is about 9.4×10^{15} ions cm^{-2} s^{-1} and the beam is characterized by an angular divergence of about $\pm 2°/3°$. We performed a set of different IBS experiments by selecting the ion beam incidence angle θ with respect to the glass substrate surface normal direction in the range of 0°−55° (see sketch in Figure 1a). A biased tungsten filament ($V_{bias} = -13$ V), providing electrons by thermoionic emission, is placed close to the extraction grid in order to compensate surface charging due to ion implantation. The substrate temperature during IBS is monitored with a K-type thermocouple placed in thermal contact with the sample holder in proximity of the sample. The glass substrate is heated up during the IBS process in a controlled way recurring to a Firerod heater, placed in thermal contact with the sample holder. The morphology of the self-organized rippled glass template has been investigated by scanning electron microscopy (SEM) with the instrument Hitachi SU3500, and by atomic force microscopy (AFM) using the instrument Nanosurf S Mobile. The slope distribution and line profile of the nanoripples are extracted from the AFM images exploiting the software WSxM.

A representative SEM image of these large-area wrinkled nanopatterns is shown in Figure 1d, where faceted ridges as long as several micrometers are clearly visible thanks to the presence of a thin Au film selectively coating one side of the asymmetric wrinkled profile (brighter regions in the SEM image). This morphology extends homogeneously over macroscopic scale (~cm^2).

2.2. PEDOT:PSS Thin Film Preparation and Characterization. PEDOT:PSS films were prepared by spin coating a PEDOT:PSS water solution (PH1000, Clevios) with 5 v/v% DMSO addition on the nanopatterned glass templates (see sketch in Figure 1b) and on flat glass substrates used as reference samples (size: ~1 cm × 1 cm). The spin coating speed used was set to 1500 and 2000 rpm. The total time for the spin coating was 2 min and the samples were annealed for 10 min at 130 °C to remove any remaining solvent trace.

AFM measurements were performed using a DI EnviroScope (Veeco) system in tapping mode acquisition at ambient temperature. For each samples, two different regions were analyzed using a scan size ranging from 1 to 20 μm. The obtained images were treated using

https://dx.doi.org/10.1021/acsanm.0c03290
ACS Appl. Nano Mater. 2021, 4, 1940−1950

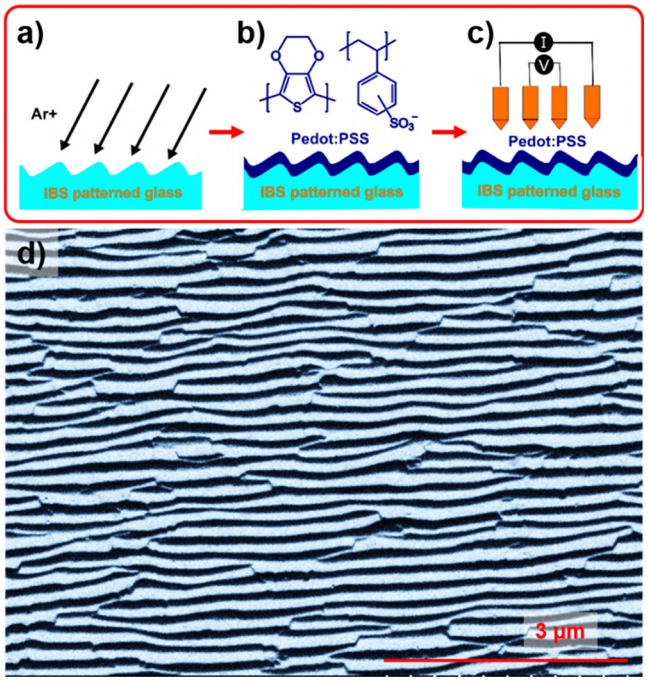

Figure 1. (a-c) Schematic view of the self-organized nanofabrication of the asymmetric faceted nanopattern, the following spin-coating of conductive thin polymer films (PEDOT:PSS) in registry with the faceted nanogrooves, and the final four-point probe conductivity measurements performed over large-area circuits, respectively. d) Scanning electron microscopy (SEM) image of the self-organized wrinkled nanopatterns. A thin Au film selectively coating only one side of the asymmetric wrinkled profile (brighter regions in the SEM image) highlight the presence of faceted ridges as long as several micrometers.

Nanoscope Analysis 1.8 (Bruker) software. A first order flattening was applied to each image to remove any background noises registered during the experiments.

The films thicknesses were measured by a profilometer (Veeco, Dektak 6M). The thickness is 90 nm for the films cast at 1500 rpm and 60 nm for the films cast at 2000 rpm.

Electrical properties for the spun cast PEDOT:PSS films were measured by using an Ossila four-point probe system (see in Figure 1c). The electrical conductivity was measured in five different regions of each sample and for three different samples of each kind in order to obtain the average value and the dispersity of the electrical conductivity. The $I-V$ curves for some of the PEDOT:PSS thin films are reported in Figure 2.

Grazing incidence wide-angle X-ray scattering (GIWAXS) measurements were performed at the multipurpose X-ray instrument for nanostructure characterization (MINA) in Groningen. The instrument is built on a Cu rotating anode providing a collimated 250 μm X-ray beam of wavelength λ = 0.15413 nm. The GIWAXS patterns were acquired using a Vantec500 Bruker detector placed 10 cm away from the sample. The thin films supported on glass substrates were placed in GIWAXS geometry and aligned at an incident angle with respect to the incoming X-ray beam of α_i = 0.25° using a Huber goniometer stage. The GIWAXS patterns originally in pixel coordinates were corrected for the so-called missing-wedge effect and converted to the parallel q_r and quasi-vertical q_z component of the scattering vectors using the GIXSGUI Matlab routine[54] and according to the following definitions

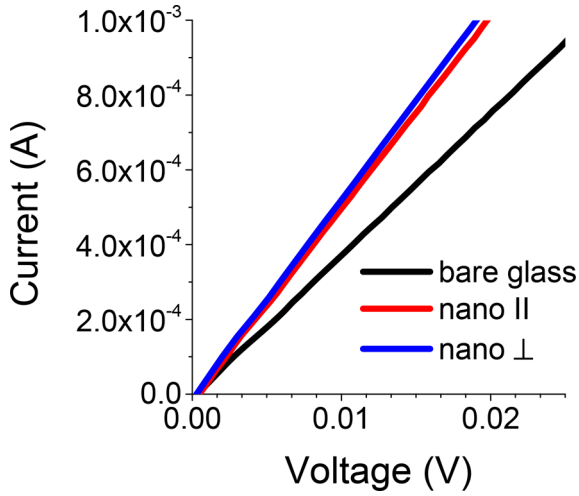

Figure 2. $I-V$ curves for (black) PEDOT:PSS:DMSO spun cast on bare flat glass and on the faceted nanostructured glass measured along (red line) and perpendicularly (blue line) with respect to the ripples direction.

$$q = \begin{cases} q_x = \frac{2\pi}{\lambda}(\cos(2\theta_f)\cos(\alpha_f) - \cos(\alpha_i)) \\ q_y = \frac{2\pi}{\lambda}(\sin(2\theta_f)\cos(\alpha_f)) \\ q_z = \frac{2\pi}{\lambda}(\sin(\alpha_i) + \sin(\alpha_f)) \end{cases}$$

where $2\theta_f$ is the scattering angle in the horizontal direction and α_f is the exit angle in the vertical direction. The parallel component of the scattering vector is thus calculated as $q_r = \sqrt{q_x^2 + q_y^2}$.

3. RESULTS AND DISCUSSION

Defocused ion beam irradiation of low-cost soda lime glass substrates heated up near the glass transition temperature, reading about 550−600 °C,[55] induces the formation of highly ordered ripple nanopatterns, as sketched in Figure 1a. These templates, shown in the SEM image of Figure 1d and in the AFM topography of Figure 3a, extend homogeneously over large-area, at the cm^2 scale. Irradiation with Ar^+ ions was performed at the off normal incidence angle θ = 30°, keeping constant the substrate temperature at about 680 K, near the glass transition point of the substrate. The process was performed for an exposure time as long as 1800 s, which corresponds to an ion fluence of about 1.4 × 10^{19} ions cm^{-2}. Under these conditions the growth of periodic ripples, endowed with enhanced vertical dynamic and lateral order, is observed. The cross-section profile extracted by the AFM images of Figure 3a and reported in Figure 3b (plot not in scale), clearly shows formation of high aspect-ratio nanoripples with typical height in the range of 60−70 nm, periodicity of about 200 nm (as confirmed by the two-dimensional (2D) self-correlation of the AFM image shown in Figure 3c), and asymmetric profile. These nanostructures show the strong amplification of the vertical dynamic of the nanopattern (up to 10-fold), selectively induced when ion irradiation is performed on glass substrates heated up near their transition point, where the substrate viscosity drops by several order of magnitude. As recently demonstrated in ref 50 under this condition a wrinkling instability can occur at the nanoscale level due to the presence of an ion-induced compressively stressed surface

https://dx.doi.org/10.1021/acsanm.0c03290
ACS Appl. Nano Mater. 2021, 4, 1940−1950

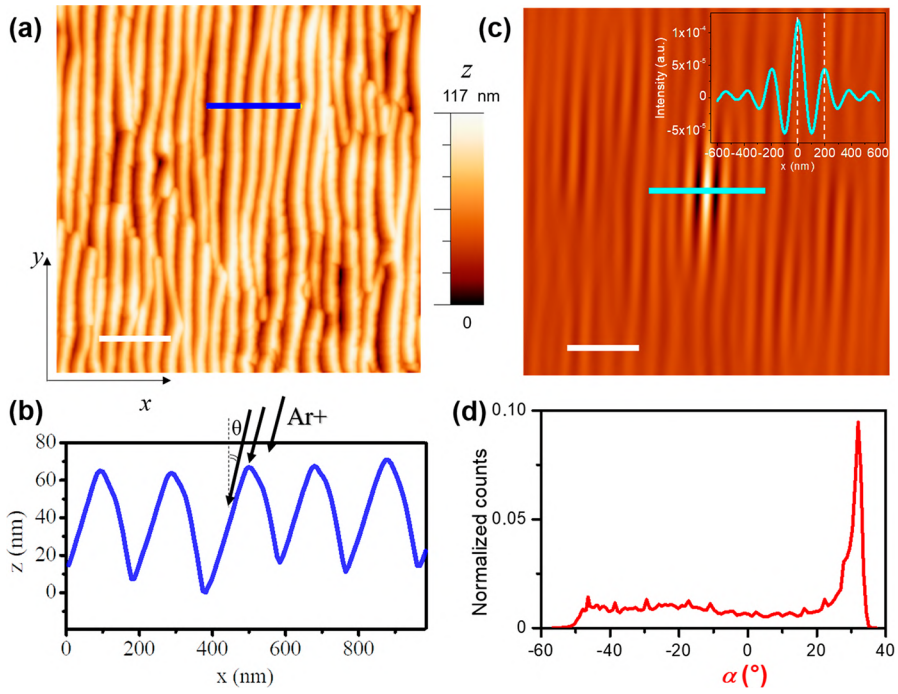

Figure 3. (a,b) AFM topography (white scale bar 800 nm) (a) and line profile (not in scale) (b) of the nanoscale wrinkled template induced on glass surfaces by ion irradiation at $\theta = 30°$ (ion fluence 1.4×10^{19} ions cm^{-2}), keeping the substrate temperature at about 680 K. (c) Two dimensional (2D) self-correlation pattern (white scale bar 800 nm) extracted from the AFM topography. The inset shows the 2D correlation profile (light-blue bar) extracted along the direction perpendicular to the wrinkles ridges, in proximity of the maximum and demonstrating a pattern periodicity of 200 nm. (d) Histogram of slopes α of the wrinkles calculated as local first derivative of the nanostructures profile dz/dx from the detected AFM image of panel (a). The counts are normalized to the integral area of the curve.

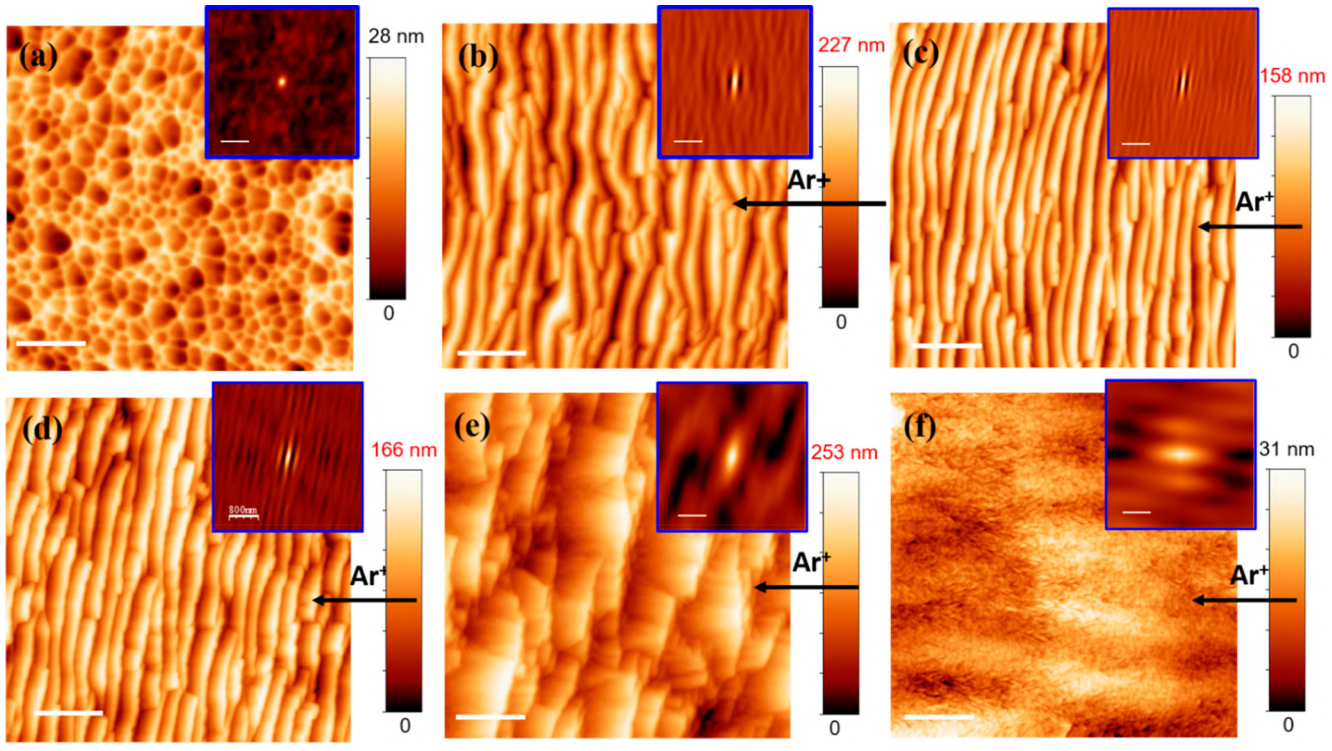

Figure 4. AFM topographies of the ripples template obtained by defocused ion beam sputtering at the substrate temperature of 680 K. All of the samples were irradiated with the same ion fluence of 1.4×10^{19} ions cm^{-2} under different ion incidence angles θ. Panels a–f correspond to experiments performed at $\theta = 0°$, 15°, 25°, 35°, 45°, and 55°, respectively. The inset of each AFM image corresponds to its 2D self-correlation pattern. All of the white scale bars correspond to 800 nm.

https://dx.doi.org/10.1021/acsanm.0c03290
ACS Appl. Nano Mater. 2021, 4, 1940–1950

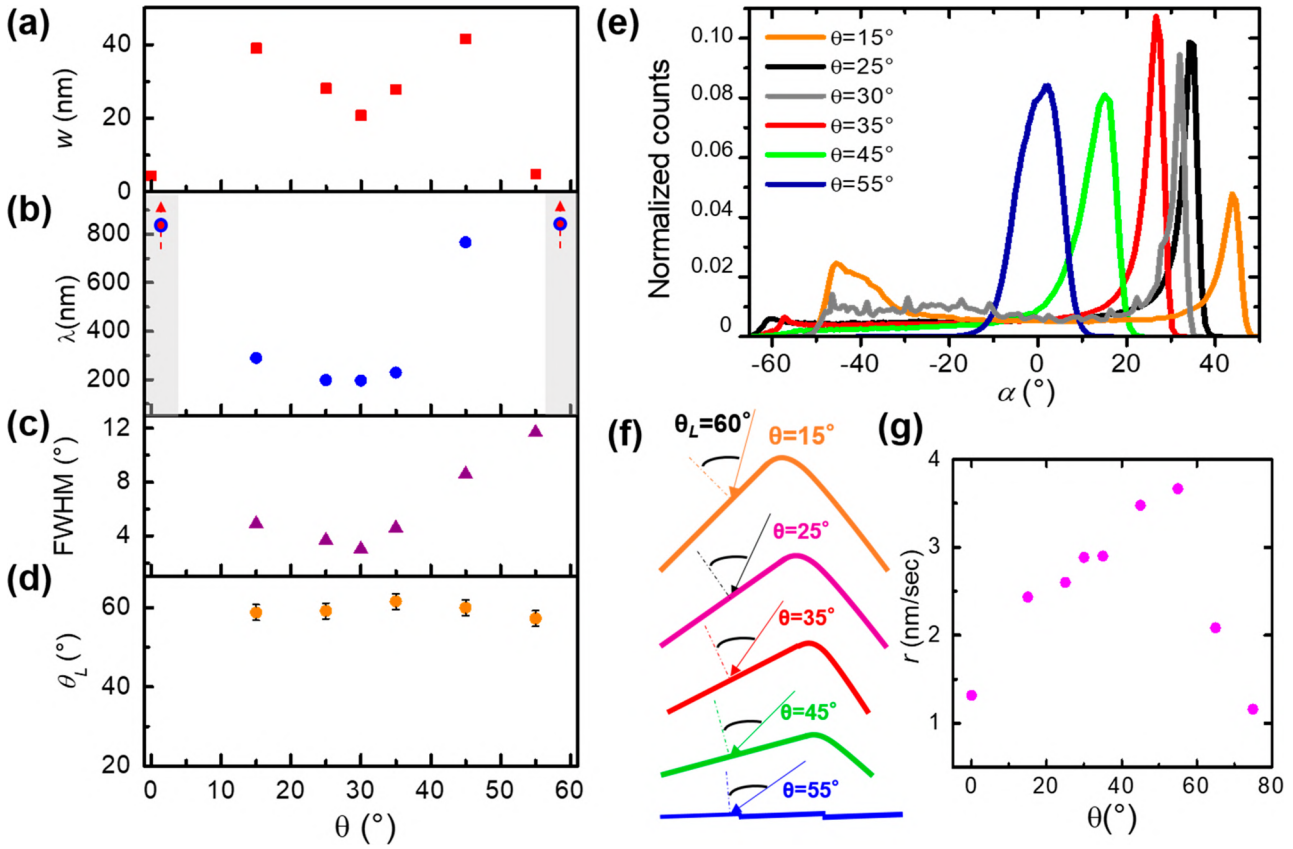

Figure 5. (a,b) RMS roughness w (red dots) and periodicity λ (blue dots) of the rippled templates plotted as a function of the ion incidence angle. (c,d) fwhm of the maximum identified in the slope distributions of panel (e) (purples dots), and local ion incidence angle θ_L on the selected facets (highlighted in the sketch of panel e) (orange dots), plotted as a function of θ. (e) Histogram of slopes corresponding to the rippled templates obtained at $\theta = 15°$ (orange line), $\theta = 25°$ (black line), $\theta = 30°$ (gray line), $\theta = 35°$ (red line), $\theta = 45°$ (green line), $\theta = 55°$ (blue line). The counts are normalized to the integral area of each curve. (f,g) Sketches of the evolution of the ripple profile, and plot of the sputtering rate measured on the same soda-lime glass as a function of θ, respectively.

layer that can effectively relax, thus enabling a strong enhancement of the vertical dynamics of the nanopattern. Additionally, a high degree of order is observed in both the SEM and the AFM image (Figures 1d and 3a, respectively) that are characterized by wrinkles as long as several micrometers, while the AFM cross-section profile (Figure 3b) highlights the presence of oriented ridges.

In order to analyze the surface topography, we calculated the histogram of the ripple slope $\alpha = \partial z/\partial x$, as the local first derivative of the nanostructures profile $z(x,y)$ with respect to the horizontal coordinate (x) (Figure 3d). The latter highlights the presence of a preferential orientation of the nanoscale ridges tilted at 30° (sharp peak in the histogram) which corresponds to the ripple facets not directly facing the ion beam. In parallel, the ripple sides facing the ion beam ($\alpha < 0°$ in Figure 3d) show a broader slope distribution extending up to 45°−50°. These features highlight the capability to achieve self-organized nanofabrication of quasi-1D periodic nanopatterns characterized by an asymmetric out-of-plane tilted profile. In order to investigate the origin of the faceting behavior and the possibility to control the facet tilt at the nanoscale, we performed a set of IBS experiments at variable ion beam incidence angle θ, while keeping fixed the substrate temperature and the ion fluence.

Under normal incidence irradiation, $\theta = 0°$ (Figure 4a), an almost flat topography is achieved (note the almost 10-fold decrease of the vertical scale bar) and the RMS surface roughness, w, drops to 4 nm with a residual contribution from an isotropic network of shallow pits. This outcome, in accordance with experimental results reported so far,[36,56] highlights the crucial role played by the ion beam direction on the evolution of a faceted nanopattern. Prevailing observations for semiconductors and oxide substrates treated by ion sputtering describe pattern formation with ridges elongated perpendicular to the ion projection only for incidence angles exceeding a critical value of around 45°,[57−59] while a region of morphological stability is found to prevail for near normal incidence angles due to the dominance of ballistic smoothing mechanisms or to relaxation induced by surface confined viscous flow.[59−61]

In this context, the glass soda lime substrate thus represents a significant anomaly since a morphological instability is observed for a low incidence angle $\theta = 30°$, as clearly demonstrated in Figure 3. In Figure 4b−e, the morphology of the rippled templates achieved after sputtering at $\theta = 15°$, 25°, 35°, and 45° are shown, respectively, after irradiation at the same ion dose. Strikingly, for incidence angles as low as $\theta = 15°$ (Figure 4b) anisotropic quasi 1D ripples are formed with a wavevector of the pattern parallel to the ion beam projection similar to the experiment of Figure 3. The AFM images clearly show that the ripple morphology is significantly affected by the ion incidence conditions with a strong improvement of lateral order and slope selection and an increase of the typical ripple length exceeding 4 μm when incidence angle is around 30°

https://dx.doi.org/10.1021/acsanm.0c03290
ACS Appl. Nano Mater. 2021, 4, 1940−1950

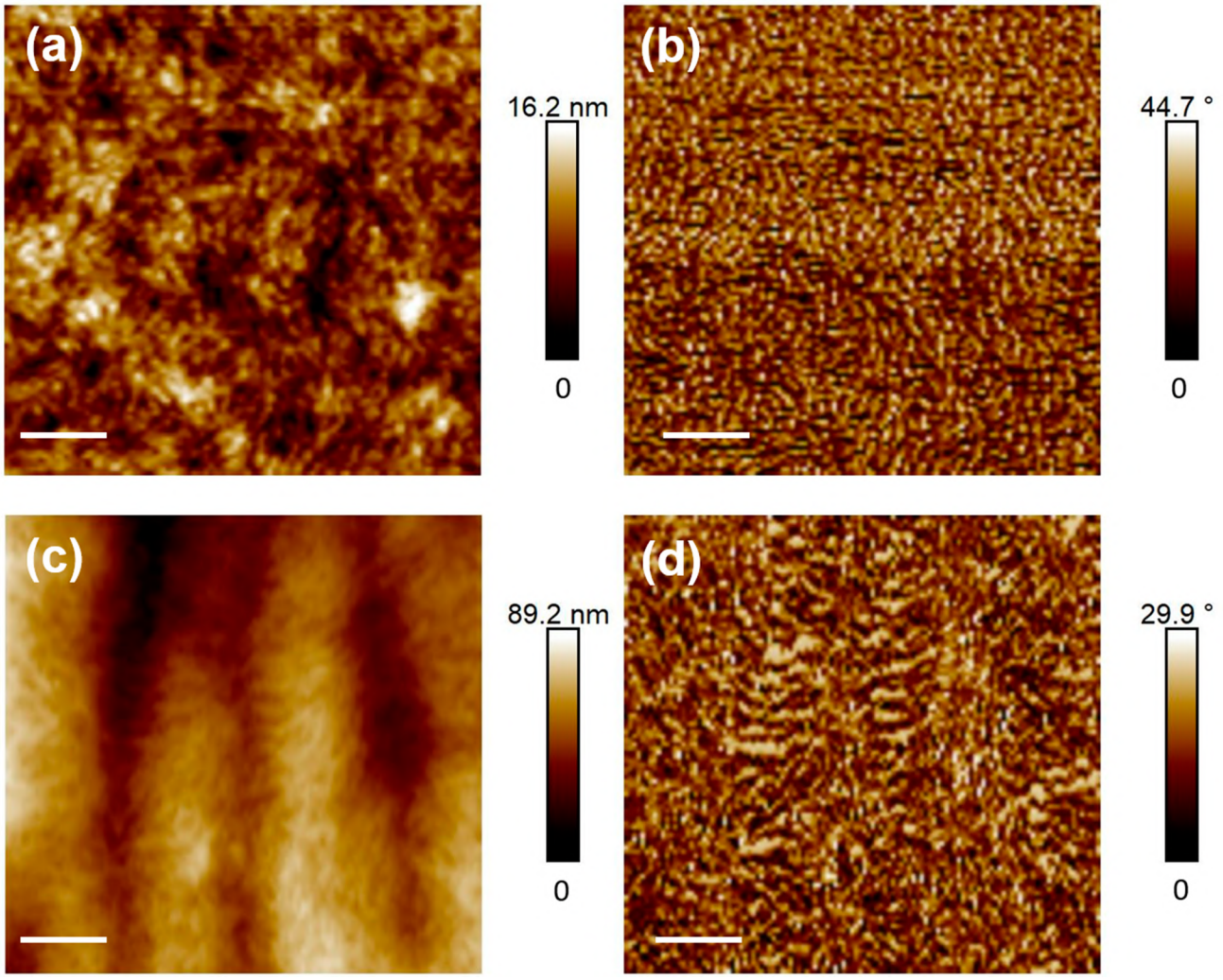

Figure 6. AFM height and phase images for the PEDOT:PSS spun cast on bare flat glass (a,b) and on the nanostructured glass (c,d). The spin coating rate used was 1500 rpm. The scan window size is 1.1 × 1.1 μm, and the white scale bars are 200 nm.

(AFM topography in Figures 3a, 4c, and 2D self-correlation images in insets of Figure 4). In a more quantitative way, in Figure 5a (upper panel) we show the evolution of the surface roughness w as a function of θ, which follows a bimodal modulation. A 10-fold roughness amplification from 4 nm up to 39 nm is observed as θ increases from 0° to 15°, followed by a slight decrease to about 27 nm in the high order region around 25° and 30°; a substantial increase of w up to 42 nm is observed when the incidence angle grows to 45°, followed by a re-entrant smoothening transition with a sharp 10-fold drop of RMS roughness to w = 4.8 nm when θ reads 55°.

For the periodicity λ (Figure 5b), determined by the cross section of the 2D self-correlation (insets of Figure 4a−f), a similar bimodal trend is observed but now the maxima are shifted to the extremes of the angular range: for θ = 0°, the wavelength diverges into a singularity (shaded area), while a minimum of λ in the range of 200 nm is found at the intermediate angle of 25°. For θ = 45° (AFM topography in Figure 4e), λ increases to 767 nm, and a substantial restructuring of the surface profile takes place: the topography is dominated by ripple facets as wide as 800 nm with a vertical amplitude of the nanopattern exceeding 200 nm. Remarkably, the surface morphology strongly changes when further tilt of the ion irradiation angle to θ = 55° is chosen (Figure 4f); under this condition the wavelength diverges and a singular plane is observed to expand across the whole surface. The lack of any rippling instability at θ = 55° suggests that peculiar ion smoothing conditions are achieved for this specific incidence angle.

In order to better understand the physical origin of this surface instability, in Figure 5e we analyzed the evolution of the nanoscale slope distribution as a function of the ion incidence angle. In the figure, we show the histograms of facet slope (α) derived from the AFM images representing the ripple pattern obtained at θ = 15° (orange line), 25° (black line), 30° (gray line), 35° (red line), 45° (green line), and 55° (blue line). These distributions highlight four main effects: (i) All of the experiments performed for θ < 55° (except for the case of 0°) lead to uniaxially faceted templates, with a strongly peaked maximum in the slope distribution at positive angles. (ii) The characteristic slope α of the selected facets, identified by the histogram maximum, is rigidly shifted in steps of 10° equivalent to the increment in ion incidence angle θ. (iii) The strong asymmetry of the slope distributions (Figures 3d, 5e) with the presence of a negative tails down to −50° demonstrates the growth of asymmetric sawtooth-like ripple profile. (iv) The slope selection process is most effective for incidence angles close to 30° (as revealed by the fwhm of the

https://dx.doi.org/10.1021/acsanm.0c03290
ACS Appl. Nano Mater. 2021, 4, 1940−1950

peak in the histogram distribution which reaches a minimum value of 3° for θ = 30°, Figure 5c.

On the basis of these observations, a slope selection mechanism driven by the local, angle-dependent erosion rate can be envisaged for positive values of the slope, which can be described in terms of the local incidence angle, θ_L, referred to ions impinging downhill on the selected facets, as sketched in Figure 5f. The plot of θ_L as a function of θ (Figure 5d) clearly highlights that the dynamic evolution of the ion-eroded surface profile selects those characteristic planes which are locally irradiated at an angle $\theta_L \approx 60°$. When the ion irradiation is performed at θ = 55° (AFM morphology in Figure 4f), the slope selected facets become parallel to the macroscopic sample plane and a singular flat facet spreads homogeneously over the whole surface. Under this condition, we thus observe a sharp drop of the surface roughness down to 4.8 nm, comparable to the surface roughness achieved by normal incidence irradiation. In order to better identify the physical origin of the observed trend, we evaluated the sputtering rate r of Ar ions impinging on the soda lime glass substrate, as a function of incidence angle θ. The parameter r is obtained by measuring the height of the erosion step in correspondence to a mask which screens the substrate from the ion flux. As shown in Figure 5g, a monotonic increase of r is observed for $0° < \theta < 55°$, followed by a maximum of about 3.7 nm/sec for θ = 55°, and by a subsequent sharp drop at more grazing irradiation angles where the ion reflection probability becomes relevant.[62] Such experimental evidence points to a crucial role of the local erosion rate in the development of the slope selection and faceting mechanism[63] in these amorphous substrates, which undergo an ion-induced wrinkling instability only at sufficiently high temperatures where surface and bulk mobility are dominant.[50] The proportionality between the increase in the observed slope and the increase of the ion incidence angle, together with the enhanced sputtering rate measured for $\theta^* \approx 55–60°$, suggests that ion erosion rate is crucial in favoring the growth of nanofacets with a local orientation $\theta_L \approx \theta^* \approx 55–60°$ with respect to the ion beam. Remarkably, this mechanism enables the easy and effective tailoring of nanofacet tilt over a large area, highlighting a strong potential of these templates in optoelectronics and nanoelectronics.

The peculiar asymmetric sawtooth profile observed suggests that additional nonlinear instabilities should be considered and play a significant role, as demonstrated in recent theoretical studies;[33,48] so far, however, a one-to-one comparison of the experimental and simulation parameters is not at hand.

With the aim to move toward possible applications, and in order to show the potential of this self-organized platforms, we explored here the capability of these faceted large area glass templates to alter and steer the nanoscale structure of conducting polymers useful for organic electronics applications. PEDOT:PSS is one of the most promising conducting polymers with wide applications in flexible electronics. In water suspensions, insoluble PEDOT chains are complexed by the hydrophilic PSS to form water-soluble elongated micelles.[64] Upon solution casting, the micelles aggregate and the system phase separates into PEDOT nanocrystals embedded in a free PSS matrix.[65] Addition of polar cosolvents such as DMSO and DMF can improve PEDOT crystallization and promotes phase separation, forming a network of elongated crystalline aggregates and allowing PEDOT:PSS thin films to reach conductivities of the order of 500–1000 S/cm.[66]

Of paramount importance for the final electrical properties is the orientation of the PEDOT crystals, whose nature can be either face-on (FO, i.e., the aromatic PEDOT units lie parallel with respect to the substrate) or edge-on (EO, i.e., the aromatic PEDOT units lie perpendicular with respect to the substrate).[66,67] Because of its very good transparency in thin films (>90%), deposition of PEDOT:PSS on glass substrates is very often used in organic photovoltaic and organic light-emitting diode devices.[68] Moreover, the production of nanostructured PEDOT:PSS surfaces is interesting for different organic electronic devices and this is commonly achieved by expensive and multistep photolithography methods.[69] Thus, the use of nonexpensive solution-based methods to obtain nanostructured PEDOT:PSS films is desired.

In Figure 6a–d, we report the AFM images of PEDOT:PSS thin films deposited by spin coating at 1500 rpm from a 5% DMSO in water suspension on a bare flat glass and on a faceted glass template, like the one shown in Figure 4c. The latter was prepared by ion beam sputtering at θ = 25° and is characterized by periodic faceted ridges oriented at about 35° slope. Generally, our AFM investigation did not show sign of holes and dewetted regions, suggesting that high quality PEDOT:PSS films with homogeneous coverage can be achieved on the faceted templates. AFM analysis of the film deposited on flat glass shows randomly oriented PEDOT nanocrystals, easily discernible as the brighter objects in the AFM phase images (Figure 6b). These nanocrystals tend to aggregate into slightly elongated short nanofibrils, as reported for films processed from water in the presence of DMSO.[65] When deposited on the nanopatterned substrate, the polymeric film tends to reproduce the wrinkled structure, as it can be seen in the topographic AFM image in Figure 6c. Interestingly, the film deposited on the faceted glass template shows an improved well-developed fibrillar structure with larger nanodomains and with some level of preferred orientation clearly visible in the AFM phase image shown in Figure 6d. The preferential orientation seems to be higher in the regions in between the wrinkles where the elongated crystals appear to have grown with their long axis perpendicular to the wrinkles. This observation may suggest that PEDOT crystal nucleation has occurred on the wrinkle edges, followed by directional growth. A well-developed and interconnected fibrillar PEDOT structure is usually responsible for an increase of the electrical conductivity. Electrical conductivity of the thin film was here measured along two directions, respectively, oriented parallel ($\sigma_\parallel$) and perpendicular ($\sigma_\perp$) to main axis of the wrinkled substrate (see Figure 2 and relative text in Experimental Section). As a result of the anisotropic growth observed by AFM, we record a slight but significant electrical anisotropy, with directional conductivity values reading $\sigma_\parallel$ = 1020 ± 20 S/cm and $\sigma_\perp$ = 1130 ± 30 S/cm, both sensibly higher than the value of σ = 795 ± 15 S/cm measured for the film deposited on the bare flat glass. This effect seems to be also slightly thickness dependent but robust against the used spin coating conditions. When the film is spun cast on the same glass nanopattern at 2000 rpm from a 5% DMSO in water suspension, the measured electrical anisotropy was $\sigma_\parallel$ = 960 ± 20 S/cm and $\sigma_\perp$ = 1010 ± 20 S/cm, whereas the conductivity for the thin film deposited with the same conditions on flat glass was 630 ± 20 S/cm. In order to further confirm the structural anisotropy of the PEDOT:PSS film deposited on the faceted glass, we have also performed grazing incidence wide-angle X-ray scattering analysis

https://dx.doi.org/10.1021/acsanm.0c03290
ACS Appl. Nano Mater. 2021, 4, 1940–1950

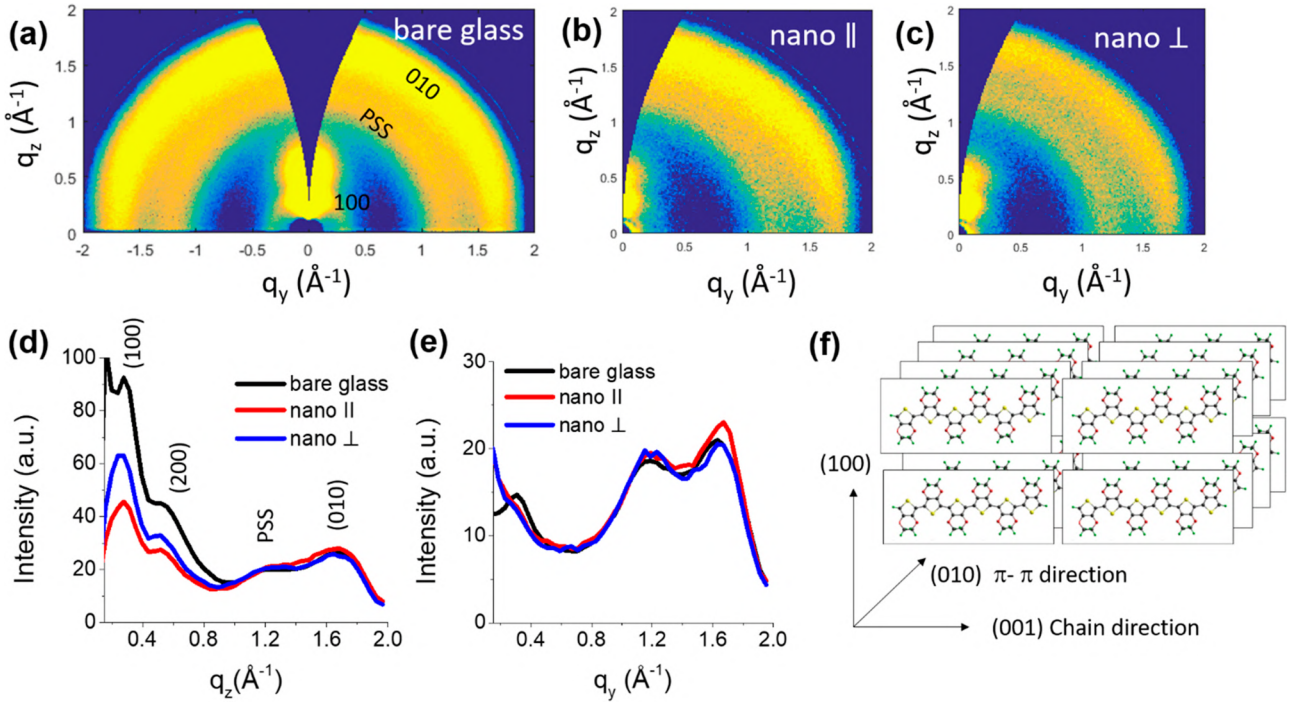

Figure 7. Wedge-corrected GIWAXS patterns for the PEDOT:PSS spun cast at 1500 rpm on (a) bare flat glass; (b) nanostructured glass with the X-ray aligned parallel to the wrinkled structures and (c) nanostructured glass with the X-ray aligned perpendicular to the wrinkled structures. The extracted intensity cuts along the horizontal q_y and vertical q_z directions are reported in (d,e), respectively. (f) Scheme for the edge-on (EO) PEDOT crystallites with the respective crystallographic axis. The PSS chains are not depicted here.

(GIWAXS, see Figure 7a–e). A clear effect of the nanostructured glass on the PEDOT crystallite orientation is observed by comparing the GIWAXS patterns for the film deposited on bare flat glass (Figure 7a) with the ones for the film deposited on the nanostructured glass (Figure 7b,c).

As a diagnostic peak, we can first consider the (100) peak located around $q_{y/z}$ = 0.28 nm^{-1} and related to the lateral PEDOT interchain stacking inside the crystals (see Figure 7f). For PEDOT:PSS deposited on bare flat glass, the (100) peak consists of a contribution from PEDOT crystallites oriented in an edge-on (EO) fashion, scattering along the q_z direction, and isotropically oriented crystallites, providing a continuous ring signal (see Figure 7a). As a result, the (100) peak is observed in both the q_z and q_y direction (black curves in Figure 7d,e). On the contrary, when PEDOT:PSS is deposited on the nanostructured substrate (Figure 7b,c), the isotropic signal is practically absent, suggesting stabilization of edge-on (EO) alignment of the PEDOT crystals and suppression of the isotopically oriented crystals on the nanostructured glass.

Moreover, GIWAXS patterns acquired with the X-rays oriented perpendicular to the wrinkles (Figure 7b) show an increase in the intensity of the (100) peak along the vertical q_z direction with respect to the parallel direction (Figure 7d), suggesting that the EO crystallites have grown preferentially perpendicularly to the wrinkles. The increase in population of the EO-oriented PEDOT crystals positively influences the electrical conductivity, especially along the direction perpendicular to the wrinkles. Also, with the lower diffuse scattering due to structural disorder observed at low q_z-values, the better defined shape of the (100) peak and the increased (010) peak related to a better $\pi-\pi$ stacking of the PEDOT chains intensity (particularly observed along the q_y direction and with the X-rays aligned along the wrinkles) indicate the higher degree of order for the films deposited on the nanostructured glass. These observations explain well the increase in the overall film conductivity measured for the system deposited on the nanostructured substrate as discussed above. It thus seems clear that the faceted substrate alters the structure in PEDOT:PSS thin films, inducing better ordering and preferential alignment of the PEDOT crystals. This could be the result of a preferential interaction of PEDOT crystals on the faceted periodic nanostructures or the result of a difference in the wettability of the PEDOT:PSS solution on the faceted substrate, as this was proven to be important for other PEDOT:PSS-based systems.[70] Full understanding of the mechanism of growth of PEDOT crystals on faceted surfaces is outside the scope of this manuscript and future upcoming work will specifically addresses the aspects of this intriguing templated growth of polymeric thin films on the faceted glass substrates. We stress that the large area templates endowed with slope-selected facets here described are of potential interest in a broad range of applications ranging from plasmonics, flat-optics, and plasmon-enhanced spectroscopies[12,19,51] to nonlinear optics[9,10] and optoelectronics.[21,50]

4. CONCLUSIONS

We showed the self-organized nanofabrication of large-area (cm^2 scale) nanopatterns at the surface of low-cost amorphous substrates via ion-induced wrinkling. We achieved the controlled growth of 1D arrays based on high aspect-ratio faceted ridges, as long as several micrometers. These wrinkle facets are endowed with selected out-of-plane tilt which is tunable at will by simply changing the macroscopic ion beam incidence angle on the sample surface. By performing a set of experiments under different ion irradiation conditions, we demonstrated that a slope-selection mechanism promotes the

https://dx.doi.org/10.1021/acsanm.0c03290
ACS Appl. Nano Mater. 2021, 4, 1940–1950

growth of nanofacets with a local tilt of about 60° with respect to the ion beam direction. The latter condition in turn corresponds to the maximum in the angle-dependent erosion velocity of the substrate. In this way, the growth of an asymmetric sawtooth profile is promoted. The peculiar and tunable features of these faceted nanopatterns qualify them as ideal templates for cost-effective optolectronic and nanoelectronic applications. Here, we demonstrate the strong potential of these nanostructured templates in the field of organic electronics by triggering anisotropic crystallization of thin PEDOT:PSS films spun cast on top of the nanopatterned templates. In turn, the anisotropy in the PEDOT crystal orientation induces an anisotropic enhancement of conductivity with an overall increase in conductivity of ∼60% in comparison to flat reference films processed from solution under comparable conditions on planar templates. The results reported here hold promise in altering the transport properties of conducting polymers and other small conducting organic molecules in an inexpensive way.

AUTHOR INFORMATION

Corresponding Authors

Francesco Buatier de Mongeot − *Dipartimento di Fisica, Università di Genova, 16146 Genova, Italy;* orcid.org/0000-0002-8144-701X; Email: buatier@fisica.unige.it

Giuseppe Portale − *Macromolecular Chemistry and New Polymeric Materials, Zernike Institute for Advanced Materials, University of Groningen, 9747 AG Groningen, The Netherlands;* orcid.org/0000-0002-4903-3159; Email: g.portale@rug.nl

Authors

Maria Caterina Giordano − *Dipartimento di Fisica, Università di Genova, 16146 Genova, Italy;* orcid.org/0000-0002-9757-4339

Federico di Sacco − *Macromolecular Chemistry and New Polymeric Materials, Zernike Institute for Advanced Materials, University of Groningen, 9747 AG Groningen, The Netherlands;* orcid.org/0000-0002-8700-6151

Matteo Barelli − *Dipartimento di Fisica, Università di Genova, 16146 Genova, Italy;* orcid.org/0000-0002-3960-7921

Complete contact information is available at: https://pubs.acs.org/10.1021/acsanm.0c03290

Notes

The authors declare no competing financial interest.

ACKNOWLEDGMENTS

Financial support is gratefully acknowledged from Ministero dell'Universitá e della Ricerca Scientifica (MIUR) through the PRIN 2015 Grant 2015WTW7J3 from Compagnia di San Paolo in the framework of Project ID ROL 9361. R.Chittofrati is acknowledged for providing technical assistance in the nanofabrication tasks. J. Dong is acknowledged for stimulating scientific discussions and his help in the electrical measurements. L. De Jong is acknowledged for the help with the polymer film preparation and the assistance with the X-ray data.

REFERENCES

(1) Liu, M.; Pu, X.; Jiang, C.; Liu, T.; Huang, X.; Chen, L.; Du, C.; Sun, J.; Hu, W.; Wang, Z. L. Large-area all-textile pressure sensors for monitoring human motion and physiological signals. *Adv. Mater.* **2017**, *29*, 1703700.

(2) Zakharov, A. A.; Vinogradov, N. A.; Aprojanz, J.; Nhung Nguyen, T. T.; Tegenkamp, C.; Struzzi, C.; Iakimov, T.; Yakimova, R.; Jokubavicius, V. Wafer Scale Growth and Characterization of Edge Specific Graphene Nanoribbons for Nanoelectronics. *ACS Appl. Nano Mater.* **2019**, *2* (1), 156−162.

(3) Belushkin, A.; Yesilkoy, F.; González-López, J. J.; Ruiz-Rodríguez, J. C.; Ferrer, R.; Fàbrega, A.; Altug, H. Rapid and Digital Detection of Inflammatory Biomarkers Enabled by a Novel Portable Nanoplasmonic Imager. *Small* **2020**, *16*, 1906108.

(4) Sprinkle, M.; Ruan, M.; Hu, Y.; Hankinson, J.; Rubio-Roy, M.; Zhang, B.; Wu, X.; Berger, C.; de Heer, W. A. Scalable templated growth of graphene nanoribbons on SiC. *Nat. Nanotechnol.* **2010**, *5*, 727.

(5) Sun, J.; Giorgi, G.; Palummo, M.; Sutter, P.; Passacantando, M.; Camilli, L. A Scalable Method for Thickness and Lateral Engineering of 2D Materials. *ACS Nano* **2020**, *14* (4), 4861−4870.

(6) Martella, C.; Mennucci, C.; Lamperti, A.; Cappelluti, E.; de Mongeot, F. B.; Molle, A. Designer Shape Anisotropy on Transition-Metal-Dichalcogenide Nanosheets. *Adv. Mater.* **2018**, *30*, 1705615.

(7) Yu, N.; Capasso, F. Flat optics with designer metasurfaces. *Nat. Mater.* **2014**, *13*, 139.

(8) Reshef, O.; Saad-Bin-Alam, M.; Huttunen, M. J.; Carlow, G.; Sullivan, B. T.; Ménard, J. M.; Dolgaleva, K.; Boyd, R. W. Multiresonant High-Q Plasmonic Metasurfaces. *Nano Lett.* **2019**, *19* (9), 6429−6434.

(9) Belardini, A.; Benedetti, A.; Centini, M.; Leahu, G.; Mura, F.; Sennato, S.; Sibilia, C.; Robbiano, V.; Giordano, M. C.; Martella, C.; Comoretto, D.; Buatier de Mongeot, F. Second harmonic generation circular dichroism from self-ordered hybrid plasmonic-photonic nanosurfaces. *Adv. Opt. Mater.* **2014**, *2*, 208.

(10) Belardini, A.; Larciprete, M. C.; Centini, M.; Fazio, E.; Sibilia, C.; Chiappe, D.; Martella, C.; Toma, A.; Giordano, M.; Buatier de Mongeot, F. Circular dichroism in the optical second-harmonic emission of curved gold metal nanowires. *Phys. Rev. Lett.* **2011**, *107*, 257401.

(11) Fleischman, D.; Fountaine, K. T.; Bukowsky, C. R.; Tagliabue, G.; Sweatlock, L. A.; Atwater, H. A. High spectral resolution plasmonic color filters with subwavelength dimensions. *ACS Photonics* **2019**, *6*, 332.

(12) Giordano, M. C.; Longhi, S.; Barelli, M.; Mazzanti, A.; Buatier de Mongeot, F.; Della Valle, G. Plasmon hybridization engineering in self-organized anisotropic metasurfaces. *Nano Res.* **2018**, *11*, 3943.

(13) Peinado, A.; Kildemo, M.; Aas, L.M. S.; Martella, C.; Giordano, M. C.; Chiappe, D.; Buatier de Mongeot, F.; Borondics, F.; Garcia-Caurel, E. IR-Mueller matrix ellipsometry of self-assembled nanopatterned gold grid polarizer. *Appl. Surf. Sci.* **2017**, *421*, 728.

(14) Smalley, J. S. T.; Vallini, F.; Montoya, S. A.; Ferrari, L.; Shahin, S.; Riley, C. T.; Kanté, B.; Fullerton, E.; Liu, Z.; Fainman, Y. Luminescent hyperbolic metasurfaces. *Nat. Commun.* **2017**, *8*, 13793.

(15) Yang, J.; Wang, Z.; Wang, F.; Xu, R.; Tao, J.; Zhang, S.; Qin, Q.; Luther-Davies, B.; Jagadish, C.; Yu, Z.; Lu, Y. Atomically thin optical lenses and gratings. *Light: Sci. Appl.* **2016**, *5*, No. e16046.

(16) Wu, J.; Zhao, H.; Li, Y.; Ohlberg, D.; Shi, W.; Wu, W.; Wang, H.; Tan, P. Monolayer molybdenum disulfide nanoribbons with high optical anisotropy. *Adv. Opt. Mater.* **2016**, *4*, 756.

(17) Rodrigo, D.; Limaj, O.; Janner, D.; Etezadi, D.; Garcia de Abajo, F. J.; Pruneri, V.; Altug, H. Mid-infrared plasmonic biosensing with graphene. *Science* **2015**, *349*, 165.

(18) Kufer, D.; Konstantatos, G. Highly sensitive, encapsulated MoS2 photodetector with gate controllable gain and speed. *Nano Lett.* **2015**, *15*, 7307.

(19) Giordano, M. C.; Tzschoppe, M.; Barelli, M.; Vogt, J.; Huck, C.; Canepa, F.; Pucci, A.; Buatier de Mongeot, F. Self-Organized Nanorod Arrays for Large-Area Surface-Enhanced Infrared Absorption. *ACS Appl. Mater. Interfaces* **2020**, *12*, 11155.

(20) Repetto, D.; Giordano, M. C.; Martella, C.; Buatier de Mongeot, F. *Appl. Surf. Sci.* **2015**, *327*, 444.

(21) Giordano, M. C.; Repetto, D.; Mennucci, C.; Carrara, A.; Buatier de Mongeot, F. Template-assisted growth of transparent plasmonic nanowire electrodes. *Nanotechnology* **2016**, *27*, 495201.
(22) Xue, Y.; Chen, S.; Yu, J.; Bunes, B. R.; Xue, Z.; Xu, J.; Lu, B.; Zang, L. Nanostructured conducting polymers and their composites: synthesis methodologies, morphologies and applications. *J. Mater. Chem. C* **2020**, *8* (30), 10136−10159.
(23) Shi, H.; Liu, C.; Jiang, Q.; Xu, J. Effective approaches to improve the electrical conductivity of PEDOT: PSS: a review. *Adv. Electron. Mater.* **2015**, *1* (4), 1500017.
(24) Gerard, M. Application of conducting polymers to biosensors. *Biosens. Bioelectron.* **2002**, *17*, 345.
(25) Nambiar, S.; Yeow, J. T. W. Conductive polymer-based sensors for biomedical applications. *Biosens. Bioelectron.* **2011**, *26*, 1825.
(26) Gong, M.; Zhang, L.; Wan, P. Polymer nanocomposite meshes for flexible electronic devices. *Prog. Polym. Sci.* **2020**, *107*, 101279.
(27) El Gemayel, M.; Narita, A.; Dossel, L. F.; Sundaram, R. S.; Kiersnowski, A.; Pisula, W.; Hansen, M. R.; Ferrari, A. C.; Orgiu, E.; Feng, X.; Mullen, K.; Samori, P. Graphene nanoribbon blends with P3HT for organic electronics. *Nanoscale* **2014**, *6* (12), 6301.
(28) Rammohan, A.; Dwivedi, P. K.; Martinez-Duarte, R.; Katepalli, H.; Madou, M. J.; Sharma, A. One-step maskless grayscale lithography for the fabrication of 3-dimensional structures in SU-8 Sensors. *Sens. Actuators, B* **2011**, *153*, 125.
(29) Eschimese, D.; Vaurette, F.; Troadec, D.; Leveque, G.; Melin, T.; Arscott, S. Size and shape control of a variety of metallic nanostructures using tilted, rotating evaporation and lithographic lift-off techniques. *Sci. Rep.* **2019**, *9* (1), 1−9.
(30) Boles, M. A.; Engel, M.; Talapin, D. V. Self-assembly of colloidal nanocrystals: from intricate structures to functional materials. *Chem. Rev.* **2016**, *116*, 11220.
(31) Giordano, M. C.; Foti, A.; Messina, E.; Gucciardi, P. G.; Comoretto, D.; Buatier de Mongeot, F. SERS amplification from self-organized arrays of plasmonic nanocrescents. *ACS Appl. Mater. Interfaces* **2016**, *8*, 6629.
(32) Chan, W. L.; Chason, E. Making waves: kinetic processes controlling surface evolution during low energy ion sputtering. *J. Appl. Phys.* **2007**, *101*, 121301.
(33) Pearson, D. A.; Bradley, R. M. Theory of terraced topographies produced by oblique-incidence ion bombardment of solid surfaces. *J. Phys.: Condens. Matter* **2015**, *27*, 015010.
(34) Norris, S. A.; Aziz, M. J. Ion-induced nanopatterning of silicon: Toward a predictive model. *Appl. Phys. Rev.* **2019**, *6*, 011311.
(35) Herbig, C.; Michely, T. Graphene: the ultimately thin sputtering shield. *2D Mater.* **2016**, *3*, 025032.
(36) Valbusa, U.; Boragno, C.; Buatier de Mongeot, F. Nano-structuring surfaces by ion sputtering. *J. Phys.: Condens. Matter* **2002**, *14*, 8153.
(37) Makeev, M. A.; Cuerno, R.; Barabási, A. L. Morphology of ion-sputtered surfaces. *Nucl. Instrum. Methods Phys. Res., Sect. B* **2002**, *197*, 185.
(38) Rusponi, S.; Boragno, C.; Valbusa, U. Ripple structure on Ag (110) surface induced by ion sputtering. *Phys. Rev. Lett.* **1997**, *78*, 2795.
(39) Mussi, V.; Granone, F.; Boragno, C.; Buatier de Mongeot, F.; Valbusa, U.; Marolo, T.; Montereali, R. M. Surface nanostructuring and optical activation of lithium fluoride crystals by ion beam irradiation. *Appl. Phys. Lett.* **2006**, *88*, 103116.
(40) Ou, X.; Keller, A.; Helm, M.; Fassbender, J.; Facsko, S. Reverse epitaxy of Ge: ordered and faceted surface patterns. *Phys. Rev. Lett.* **2013**, *111*, 016101.
(41) Oates, T. W. H.; Keller, A.; Facsko, S.; Mücklich, A. Aligned silver nanoparticles on rippled silicon templates exhibiting anisotropic plasmon absorption. *Plasmonics* **2007**, *2*, 47.
(42) Chowdhury, D.; Ghose, D. Ar+-sputtered Ge (001) surface nanostructuring at target temperature above the recrystallization threshold. *J. Phys. D: Appl. Phys.* **2020**, *53*, 335304.
(43) Bai, S.; Li, X.; Kong, Q.; Long, R.; Wang, C.; Jiang, J.; Xiong, Y. Toward enhanced photocatalytic oxygen evolution: synergetic utilization of plasmonic effect and schottky junction via interfacing facet selection. *Adv. Mater.* **2015**, *27*, 3444.
(44) Liu, G.; Wang, T.; Zhou, W.; Meng, X.; Zhang, H.; Liu, H.; Kako, T.; Ye, J. Crystal-facet-dependent hot-electron transfer in plasmonic-Au/semiconductor heterostructures for efficient solar photocatalysis. *J. Mater. Chem. C* **2015**, *3*, 7538.
(45) Carter, G. The physics and applications of ion beam erosion. *J. Appl. Phys.* **1999**, *85*, 455.
(46) Basu, T.; Datta, D.; Som, T. Transition from ripples to faceted structures under low-energy argon ion bombardment of silicon: understanding the role of shadowing and sputtering. *Nanoscale Res. Lett.* **2013**, *8*, 289.
(47) Engler, M.; Macko, S.; Frost, F.; Michely, T. Evolution of ion beam induced patterns on Si (001). *Phys. Rev. B: Condens. Matter Mater. Phys.* **2014**, *89*, 245412.
(48) Loew, K. M.; Bradley, R. M. Effect of dispersion on the nanoscale patterns produced by ion sputtering. *Phys. Rev. E: Stat. Phys., Plasmas, Fluids, Relat. Interdiscip. Top.* **2019**, *100*, 012801.
(49) Zeng, S.; Li, R.; Freire, S. G.; Garbellotto, V. M. M.; Huang, E. Y.; Smith, A. T.; Hu, C.; Tait, W. R. T.; Bian, Z.; Zheng, G.; Zhang, D.; Sun, L. Moisture-responsive wrinkling surfaces with tunable dynamics. *Adv. Mater.* **2017**, *29* (24), 1700828.
(50) Giordano, M. C.; Buatier de Mongeot, F. Anisotropic Nanoscale Wrinkling in Solid-State Substrates. *Adv. Mater.* **2018**, *30*, 1801840.
(51) Barelli, M.; Mazzanti, A.; Giordano, M. C.; Della Valle, G.; Buatier de Mongeot, F. Color Routing via Cross-Polarized Detuned Plasmonic Nanoantennas in Large Area Metasurfaces. *Nano Lett.* **2020**, *20*, 4121.
(52) Groenendaal, L.; Jonas, F.; Freitag, D.; Pielartzik, H.; Reynolds, J. R. Poly (3, 4-ethylenedioxythiophene) and its derivatives: past, present, and future. *Adv. Mater.* **2000**, *12*, 481.
(53) Zhang, P.; Reiser, B.; González-García, L.; Beck, S.; Drzic, J.; Kraus, T. Drying of electrically conductive hybrid polymer-gold nanorods studied with in situ microbeam GISAXS. *Nanoscale* **2019**, *11* (14), 6538.
(54) Jiang, Z. GIXSGUI: a MATLAB toolbox for grazing-incidence X-ray scattering data visualization and reduction, and indexing of buried three-dimensional periodic nanostructured films. *J. Appl. Crystallogr.* **2015**, *48*, 917.
(55) Hulsenberg, D.; Harnisch, A.; Bismarck, A. *Microstructuring of Glasses*; Springer Series in Material Science; Springer: Berlin, 2008; Vol. *87*.
(56) Moreno-Barrado, A.; Castro, M.; Gago, R.; Vázquez, L.; Muñoz-García, J.; Redondo-Cubero, A.; Galiana, B.; Ballesteros, C.; Cuerno, R. Nonuniversality due to inhomogeneous stress in semiconductor surface nanopatterning by low-energy ion-beam irradiation. *Phys. Rev. B: Condens. Matter Mater. Phys.* **2015**, *91*, 155303.
(57) Bradley, R. M.; Harper, J. M. E. Theory of ripple topography induced by ion bombardment. *J. Vac. Sci. Technol., A* **1988**, *6*, 2390.
(58) Madi, C. S.; Aziz, M. Multiple scattering causes the low energy-low angle constant wavelength topographical instability of argon ion bombarded silicon surfaces. *Appl. Surf. Sci.* **2012**, *258*, 4112.
(59) Castro, M.; Gago, R.; Vázquez, L.; Muñoz-García, J.; Cuerno, R. Stress-induced solid flow drives surface nanopatterning of silicon by ion-beam irradiation. *Phys. Rev. B: Condens. Matter Mater. Phys.* **2012**, *86*, 214107.
(60) Carter, G.; Vishnyakov, V. Roughening and ripple instabilities on ion-bombarded SiPhys. *Phys. Rev. B: Condens. Matter Mater. Phys.* **1996**, *54*, 17647.
(61) Harrison, M. P.; Bradley, R. M. Crater function approach to ion-induced nanoscale pattern formation: Craters for flat surfaces are insufficient. *Phys. Rev. B: Condens. Matter Mater. Phys.* **2014**, *89*, 245401.
(62) Sigmund, P. Theory of sputtering. I. Sputtering yield of amorphous and polycrystalline targets. *Phys. Rev.* **1969**, *184*, 383.

https://dx.doi.org/10.1021/acsanm.0c03290
ACS Appl. Nano Mater. 2021, 4, 1940−1950

(63) Carter, G.; Colligon, J. S.; Nobes, M. J. The equilibrium topography of sputtered amorphous solids II. *J. Mater. Sci.* **1971**, *6*, 115.
(64) Bagchi, D.; Menon, R. Conformational modification of conducting polymer chains by solvents: Small-angle X-ray scattering study. *Chem. Phys. Lett.* **2006**, *425*, 114.
(65) Takano, T.; Masunaga, H.; Fujiwara, A.; Okuzaki, H.; Sasaki, T. PEDOT nanocrystal in highly conductive PEDOT: PSS polymer films. *Macromolecules* **2012**, *45*, 3859.
(66) Dong, J.; Portale, G. Role of the Processing Solvent on the Electrical Conductivity of PEDOT: PSS. *Adv. Mater. Interfaces* **2020**, *7*, 2000641.
(67) Gueye, M. N.; Carella, A.; Faure-Vincent, J.; Demadrille, R.; Simonato, J. P. Progress in understanding structure and transport properties of PEDOT-based materials: A critical review. *Prog. Mater. Sci.* **2020**, *108*, 100616.
(68) Rippa, M.; Capasso, R.; Petti, L.; Nenna, G.; De Girolamo Del Mauro, A.; Maglione, M. G.; Minarini, C. Nanostructured PEDOT: PSS film with two-dimensional photonic quasi crystals for efficient white OLED devices. *J. Mater. Chem. C* **2015**, *3*, 147.
(69) Ouyang, S.; Xie, Y.; Wang, D.; Zhu, D.; Xu, X.; Tan, T.; Fong, H. H. Fluorescent gold nanoclusters: synthesis and recent biological application. *J. Nanomater.* **2015**, *2015*, 1.
(70) Alshammari, A. S.; Shkunov, M.; Silva, S. R. P. Correlation between wetting properties and electrical performance of solution processed PEDOT: PSS/CNT nano-composite thin films Colloid. *Colloid Polym. Sci.* **2014**, *292*, 661.

https://dx.doi.org/10.1021/acsanm.0c03290
ACS Appl. Nano Mater. 2021, 4, 1940−1950